AIAA JOURNAL
Vol. 41, No. 5, May 2003

Helmholtz Resonator Impedance Model, Part 1: Nonlinear Behavior

A. S. Hersh,* B. E. Walker,* and J. W. Celano†
Hersh Walker Acoustics, Westlake Village, California 91361

A one-dimensional preliminary design impedance prediction model is derived for Helmholtz resonators constructed with circular orifices. The model addresses only the effects of resonator geometry and incident sound-pressure amplitude. The effects of grazing flow are not included. An experimental program was conducted to calibrate unknown empirical parameters derived in the model. The model was shown to predict, reasonably accurately, impedance data published in the open literature for resonators constructed with single and multiple orifices over a wide range of sound-pressure amplitudes and frequencies. The model provides a rapid means of calculating resonator impedance as a function of resonator geometry, incident sound-pressure amplitude, and frequency.

Nomenclature

A_o	=	orifice area
A_w	=	orifice wetted area
C_D	=	acoustic discharge coefficient defined by Eq. (3)
c_0	=	speed of sound
D_c	=	cavity diameter
d_e	=	orifice inertia length defined by Eq. (19)
d_N	=	multiple-orifice diameter defined by Eq. (34)
d_o	=	single-orifice diameter
F	=	sound frequency
H	=	orifice nonlinear inertial length defined by Eq. (20) and Fig. 1
K_{ac}	=	acoustic viscous loss parameter defined by Eq. (22)
K_{ss}	=	steady-state viscous loss parameter defined by Eq. (21)
k	=	sound wave number ω/c_0
L_c	=	cavity depth
N	=	number of orifices
P_c	=	peak cavity sound pressure defined by Eq. (7)
P_{pk}	=	$\sqrt{2}P_0$
P_0	=	peak driving sound pressure acting on control volume upper surface S_o
R	=	real part of resonator impedance
R_{fd}	=	steady-state fully developed laminar resistive loss defined by Eq. (16)
R_L	=	linear resistive loss defined by Eq. (15)
r_o	=	orifice radius
S_{BL}	=	orifice boundary-layer area, $S_{BL} = S_o - S_{inv}$ defined in Fig. 1
S_c	=	cavity cross-sectional area
S_{inv}	=	orifice inviscid area defined in Fig. 1
S_N	=	multiple orifice center-to-center spacing
S_o	=	orifice area
S_w	=	orifice wetted area
t	=	time
u_{BL}	=	acoustic velocity passing through S_{BL} defined in Fig. 1
u_{inv}	=	acoustic velocity passing through S_{inv} defined in Fig. 1
u_o	=	orifice peak acoustic velocity
$\langle u_o \rangle_{rms}$	=	rms amplitude averaged over each half-cycle
V_{non}	=	nondimensional acoustic particle velocity defined by Eq. (23)
X	=	imaginary part of resonator impedance
δ	=	orifice instantaneous boundary-layer thickness
θ_p	=	phase angle between P_0 and u_o defined by Eq. (5)
κ_{vis}	=	orifice viscous loss parameter defined by Eq. (10)
λ	=	sound wavelength
μ	=	fluid viscosity
ν	=	fluid kinematic viscosity
ρ_0	=	fluid density
σ	=	orifice open area ratio, S_o/S_c
τ	=	orifice thickness
τ_w	=	acoustic shear stress acting on orifice wetted area defined by Eq. (8)
ω	=	sound radian frequency $(= 2\pi F)$

Subscripts

c	=	cavity
L	=	linear
NL	=	nonlinear
res	=	resonance

I. Introduction

RAYLEIGH credits Helmholtz as the originator of the first theoretical analysis describing the acoustic behavior of small cavity-backed resonators.[1] More recently, Junger reviewed the historical use of the Helmholtz resonator.[2] Apparently, they were used by the Greeks to provide reverberation in open-air theaters. They were also used in Swedish and Danish churches as early as the 13th century.

During the second half of the 20th century, the aircraft industry standardized the use of Helmholtz resonators to control excessive turbofan engine inlet/exhaust noise. This prompted the publication of a large number of research papers directed at understanding the basic sound energy dissipation physics of Helmholtz resonator liners as well as improved impedance prediction models.[3–26] Despite these efforts, the details of the energy dissipation mechanisms are not well understood. This is not surprising because the interaction of the sound field incident to a resonator in a flow duct application is a complicated three-dimensional, unsteady fluid mechanical problem. Further, depending on the resonator faceplate geometry, sound-pressure field, and duct mean flowfield, the flow into and out of the resonator orifice could be laminar or turbulent.

Received 11 November 2001; revision received 24 October 2002; accepted for publication 20 November 2002.

*Vice President, 780 Lakefield Road, Unit G. Member AIAA.
†Senior Engineer, 780 Lakefield Road, Unit G.

In a landmark paper Ingard and Labate conducted smoke stream flow-visualization experiments on single orifice resonators to investigate the importance of acoustic streaming.[12] They showed that four distinct circulation regions existed as a function of sound-pressure level (SPL, or equivalently orifice particle velocity) consisting of 1) outward-directed streaming at low SPL, 2) inward-directed streaming at moderate SPL, 3) pulsatory motion superimposed upon the steady circulation at SPLs between moderate and high, and 4) symmetrical pulsatory inflow/outflow at very high SPLs. They also established a connection between resonator nonlinear resistance and the translational and rotational kinetic energy of vortex rings shed from orifices.

In another landmark paper Ingard and Ising conducted a detailed experimental investigation of the nonlinear acoustic behavior of an isolated orifice.[13] They measured cavity sound pressures and sound particle velocities near the orifice (using hot wires). Test results showed that at low SPL the orifice resistance and reactance were in essential agreement with that predicted by Rayleigh's slug-mass model. At high cavity SPL, however, their measurements showed that the orifice resistance varied linearly with orifice (centerline) particle velocity and the corresponding orifice reactance decreased to almost one-half its linear value. They interpreted the orifice resistance data in terms of Bernoulli's law suggesting that the flow behavior through the orifice is quasi-steady. Their hot-wire measurements indicated that at high SPLs the flow separates at the orifice, forming a high-velocity jet. Thus during the inflow half-cycle, the flow incident to the orifice is irrotational but is highly rotational (in the form of jetting) after exiting from the orifice. During the other half of the cycle, the flow pattern is reversed. The loss of one-half of the reactance at these high pressure levels was accounted for by assuming that one-half of the end correction was "blown" away by the exiting jet. (In their experiments plate thickness was very thin; hence, most of the orifice inertia reactance is caused by end correction.) Ingard and Ising also measured the particle velocity as a function of axial distance from the orifice. They found that the inflow velocity rapidly decayed to very small values at distances of about two to three diameters from the orifice. This suggested that the near-field effects of an orifice extend only to these distances.

Yang and Cummings[14] and Cummings[15] employed a time-domain approach to investigate the acoustic behavior of orifices exposed to intense sound-pressure amplitudes. They showed that this technique naturally accounted for nonlinear interactions between the frequency components in the signal when a sound wave impacts a perforated structure. One-dimensional numerical models showed good agreement between predicted and measured results. They also showed that the loss of acoustic power at the orifice was consistent with the kinetic energy loss of two trains of ring vortices shed alternately from both sides of the orifice.

Jing and Sun investigated the nonlinear acoustic losses generated from a sharp-edged orifice exposed to intense sound.[16–18] They predicted the motion of a train of vortices shed from the orifice by deriving a discrete vortex model based upon axisymmetric potential flow. The effects of viscosity were modeled by satisfying the Kutta condition at the orifice edge. Orifice impedance was predicted based on calculating the average flow through an orifice. Results were in general agreement with measurements conducted by Cummings and Eversman.[19] Jing and Sun note that their impedance predictions do not depend on empirical vena contracta coefficients. Although this is true, the derivation used by the authors is valid only for orifices embedded in an infinite plate. To apply their model to predict the impedance of cavity-backed orifices, they would have to account for the effects of the cavity, which suppresses orifice velocity at frequencies well below and above resonance. In a series of related studies, Hirschberg and coauthors also modeled the acoustic behavior of orifices.[20–25]

Tam and Kurbatskii recently published an important demonstration of the potential of computational aeroacoustics to provide much needed insight and understanding of the behavior of Helmholtz resonator liners exposed to intense sound.[26] By solving the compressible Navier–Stokes equations governing the pumping of sound into and out of a two-dimensional slit orifice exposed to intense sound, they showed that vortex shedding controlled orifice resistive losses.

Incorporating the preceding time domain, discrete vortex and computational impedance models as wall boundary conditions in existing computationally demanding flow duct propagation/attenuation codes would impose additional computational burdens. This would further reduce their efficiency. This prompted the need to provide the aircraft engine nacelle designer with a reasonably accurate, computationally rapid, Helmholtz resonator impedance prediction model. The model is intended to be used as a preliminary design tool in tradeoff studies of liner performance vs production cost.

II. Model Derivation

The derivation of the impedance model is based on applying conservation of unsteady mass and vertical momentum across the control volume sketched in Fig. 1. The quantities o and c denote the upper and lower surfaces of the control volume, respectively. During the inflow half-cycle, the acoustic volume flow entering the resonator orifice through the upper control surface is denoted by $u_o S_o$, and the acoustic volume flow entering the cavity through the lower control surface consists of the an inviscid component, denoted by $u_{\text{inv}} S_{\text{inv}}$, and a boundary-layer component, denoted by $u_{\text{BL}} S_{\text{BL}}$.

The inflow model is valid only during the half-cycle when the incident acoustic velocity is pumped into the resonator cavity; it is not valid during the other half-cycle when the acoustic velocity is ejected from the resonator cavity. The restriction of the model to the inflow half-cycle is not unduly limiting because the particle volume flow pumped into and out of the resonator volume must be constant over a dynamically steady-state sound period. Thus an approximate solution over the inflow half-cycle should result in an approximate solution over the entire cycle. The derivation of the model assumes that all resonator dimensions are small compared to the wavelength of the incident sound field to distinguish Helmholtz resonators from quarter-wave tube resonators.

A. Conservation of Mass

Assuming $H \gg \lambda$, Tempkin has shown that to lowest order compressibility effects are small with respect to mass-flow convection.[27] With this simplification the conservation of mass flux within the control volume can be written, where u_o, u_{inv}, and u_{BL} are understood to be functions of time, as

$$u_o S_o = u_{\text{inv}} S_{\text{inv}} + u_{\text{BL}} S_{\text{BL}} \tag{1}$$

Equation (1) shows that to first order the pumping of volume flow into and out of a resonator orifice is governed by unsteady, incompressible motion. This makes sense because acoustic changes can occur only over scale lengths on the order of an acoustic wavelength.

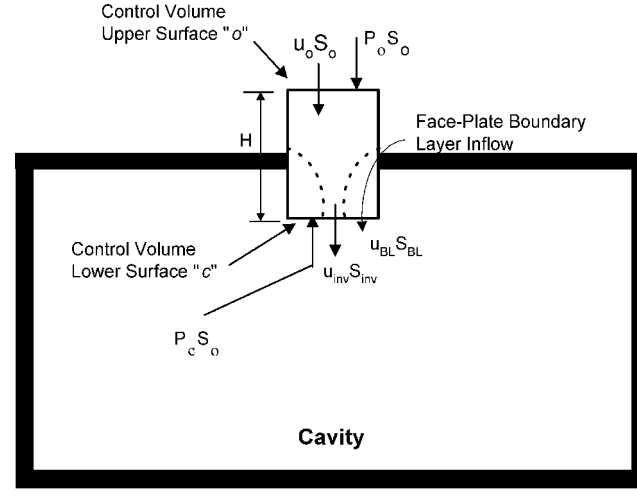

Fig. 1 Control volume used in model derivation.

B. Conservation of Vertical Momentum

Referring to Fig. 1, the conservation of momentum in the vertical direction can be written

$$\rho_0 S_o H \frac{du_o}{dt} + \rho_0 \left(u_{\text{inv}}^2 S_{\text{inv}} + u_{\text{BL}}^2 S_{\text{BL}}\right) - \rho_0 u_o^2 S_o = (P_0 - P_c) S_o - \tau_w S_w \quad (2)$$

The various terms in Eq. (2) are described here:

1) The first term on the left-hand side (LHS) represents the time rate of increase of momentum within the control volume $S_o H$. Here H is an orifice inertial length parameter that is unknown and must be modeled experimentally.

2) The second term on the LHS represents the vertical momentum flux exiting the control volume through its lower control surface.

3) The third term on the LHS represents the vertical momentum flux entering the control volume through its upper control surface.

4) The first term on the right-hand side (RHS) represents the net vertical acoustic driving force acting on the control volume. Here P_0 represents the acoustic pressure driving the sound particle volume flow into the cavity during the inflow half-cycle. Because Ingard and Ising showed that orifice near-field effects extend to about two or more orifice diameters, P_0 as defined in Fig. 1 might not accurately represent the acoustic driving pressure during the inflow half-cycle.[13] Possible errors in P_0 will be corrected empirically using the discharge coefficient concept defined next.

5) The second term on the RHS represents the momentum loss from frictional wall shear stresses τ_w distributed over the orifice-wetted area $S_w = \pi d_o \tau$.

C. Model Simplifications

The nonlinearity of Eq. (2) prevents an analytic solution. It must be solved numerically to achieve a dynamically steady-state solution, followed by a Fourier transform to calculate the fundamental harmonic velocity component. Although this procedure is numerically straightforward, it greatly complicates the design of sound-absorbing liners. Because our goal is to derive a reasonably accurate, but simple, impedance model, the following six simplifications are introduced to derive an analytic solution.

1. *Discharge Coefficient*

The first refers to the nonlinear momentum flux losses exiting the control volume through its lower control surface. Equation (2) contains the four unknown parameters u_{inv}, S_{inv}, u_{BL}, and S_{BL}, which are difficult to measure. The solution to Eq. (2) will be simplified by adapting the discharge coefficient concept used to predict one-dimensional steady-state volume flow in ducts.[28] The instantaneous inviscid volume flow $u_{\text{inv}} S_{\text{inv}}$ and boundary-layer volume flow $u_{\text{BL}} S_{\text{BL}}$ are combined into a single volume flow, denoted as $u_{\text{CD}} S_{\text{CD}}$. With this understanding Eq. (1) is written

$$u_o S_o = u_{\text{CD}} S_{\text{CD}} = u_{\text{CD}} C_D S_o, \qquad C_D \equiv S_{\text{CD}}/S_o \quad (3)$$

where u_{CD} represents the instantaneous velocity entering the cavity through an area S_{CD}. Using experimental data to determine C_D is equivalent to determining the average volume flow rate entering/exiting the resonator cavity during each half-cycle. This assumption results in the following simplification to the conservation of vertical momentum equation:

$$\rho_0 S_o H \frac{du_o}{dt} + \rho_0 \left(\frac{1 - C_D}{C_D}\right) u_o^2 S_o = (P_0 - P_c) S_o - \tau_w S_w \quad (4)$$

2. *Nonlinearity*

The second and third simplifications address the nonlinearity of Eq. (4) and are based on the hot-wire experiments of Ingard and Ising.[13] They showed, at high SPLs, the formation of alternating nonlinear jetting into and out of an orifice during each half-cycle. They also showed that the amplitudes of the higher harmonic velocity components, near resonance, were small relative to the fundamental. Physically, this permits the derivation of a model that ignores higher harmonic energy and allows for harmonic oscillation of nonlinear jetting into and out of the orifice. With this understanding the nonlinear term u_o^2 in Eq. (4) is simplified to

$$u_o^2 \cong \langle u_o \rangle_{\text{rms}} u_o(t) = \langle u_o \rangle_{\text{rms}} [u_o \exp(i\omega t + \theta_p)] \approx u_o^2 \exp(i\omega t + \theta_p) \quad (5)$$

where $\langle u_o \rangle_{\text{rms}}$ represents a time-averaged value that is proportional to the peak amplitude of the sound particle velocity over each half-cycle. Variations of the proportionality constant as a function of resonator geometry and the incident sound field will be determined empirically by absorbing it into the discharge coefficient. The phase shift θ_p between u_o and P_0 is also unknown. For frequencies at or very near resonance, $\theta_p \approx 0$. Incorporating Eq. (5) into Eq. (4) yields

$$i\rho_0 S_o(\omega H) u_o + \rho_0 [(1 - C_D)/C_D] u_o^2 S_o = (P_0 - P_c) S_o - \tau_w S_w \quad (6)$$

where the inertia term $\rho_0 S_o H \, du_o/dt$ in Eq. (4) was replaced with the expression $i\rho_0 S_o(\omega H) u_o$. The simplification achieved by ignoring higher harmonic energy permits the solution of Eq. (6) in the frequency domain rather than the time domain of Eq. (4). It is intuitively clear that at low values of SPL and/or very thick faceplates relative to orifice diameter ($\tau/d_o \gg 1$) resonator nonlinear resistive losses become negligibly small. Under these conditions the nonlinear term $(1 - C_D)/C_D$ should also become negligibly small. It should also be small at frequencies well below and above resonance where reactance dominates resistance. Test data, presented later, show that indeed $C_D \to 1$ under these conditions.

3. *Cavity Pressure*

The fourth simplification assumes that the cavity pressure can be accurately modeled by solving the one-dimensional wave equation in the cavity resulting in the following expression:

$$P_c = -i\rho_0 c_0 \sigma \cot(K L_c) u_o \quad (7)$$

4. *Viscous Scrubbing Losses*

The fifth simplification addresses the wall shear stress τ_w and assumes that it is generated by steady-state and unsteady viscous scrubbing losses. A simple model, based upon dimensional analysis, is proposed. Steady-state shear stresses are assumed to be proportional to $\mu u_o/d_o$. Acoustic shear stresses are derived assuming "Stokes-like" axially uniform diffusion of vorticity over the orifice thickness so that it is proportional to $\mu u_o \sqrt{(\omega/\nu)}$. With these assumptions the wall shear stress τ_w is written as

$$\tau_w = K_{\text{ss}} \mu (u_o/d_o) + K_{\text{ac}} \mu u_o \sqrt{\omega/\nu} \quad (8)$$

where K_{ss} and K_{ac} are unknown parameters that are functions of orifice geometry and boundary-layer flow. Substituting Eqs. (5–8) into Eq. (4) yields

$$\rho_0 [(1 - C_D)/C_D] u_o^2 S_o + \{\kappa_{\text{vis}} S_w + i\rho_0 S_o \omega_H [1 - (c_0 \sigma/\omega H) \cot(k L_c)]\} u_o = P_0 S_o \quad (9)$$

where the term κ_{vis} was introduced to simplify notation:

$$\kappa_{\text{vis}} \equiv (\mu/d_o)\left(K_{\text{ss}} + K_{\text{ac}} \sqrt{\omega d_o^2/\nu}\right) \quad (10)$$

5. *Resistance/Reactance Decoupling*

The sixth and final simplification is introduced to achieve a simple, practical solution to Eq. (9). This simplification is motivated by the impedance measurements shown in Fig. 2 for a resonator constructed with $\tau/d_o = 1$. The measurements show that near resonance resistance increases dramatically and reactance decreases moderately with SPL in agreement with the findings of Ingard and Ising.[13] At frequencies well below or above resonance, $|X|^2 \gg R^2$, which suppresses orifice jetting, thus nonlinear resistive losses are negligible. These measurements suggest that at or near resonance a resistance model can be derived that is decoupled from the effects of reactance. Because of the modest effect of SPL on reactance, well-known lumped element reactance equations are used to model reactance, modified to account for the effects of SPL. In Sec. III, empirical corrections will be used to generalize the resistance and

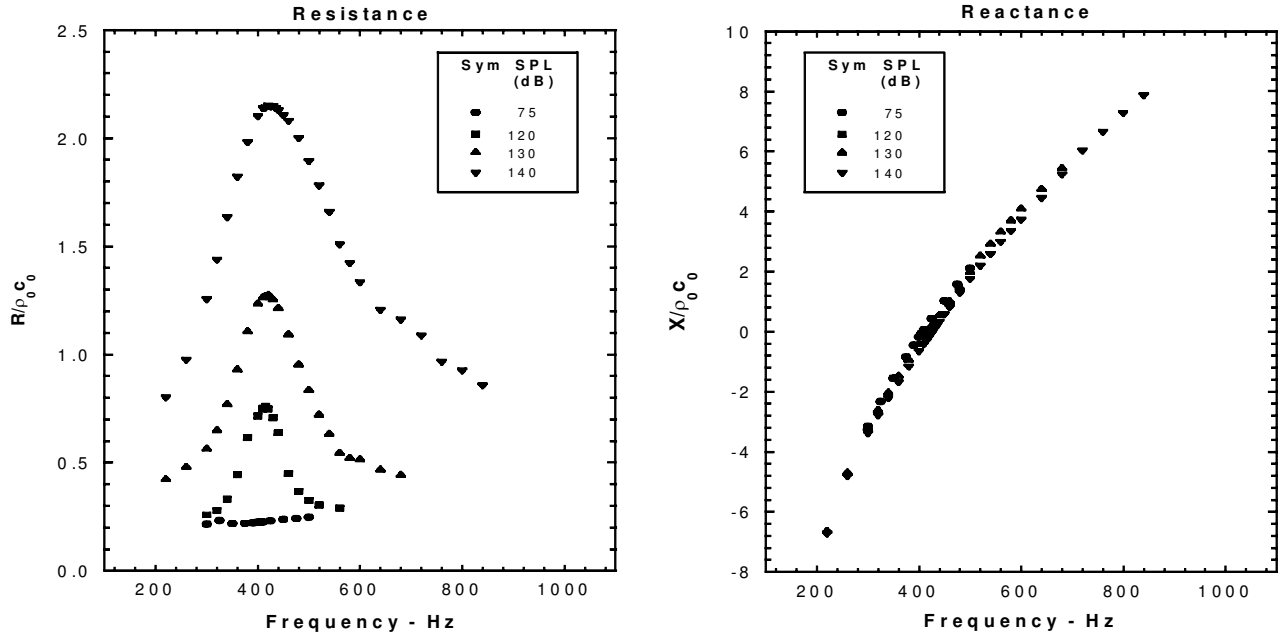

Fig. 2 Measured resonator impedance: $\tau = 0.635$ cm, $d_o = 0.635$ cm, $L_c = 2.54$ cm, and $D_c = 5.08$ cm.

reactance models over a wide range of frequencies below and above resonance.

Tuned resistance. Near resonance Eq. (9) simplifies to

$$\rho_0 S_o[(1 - C_D)/C_D]u_o^2 + \kappa_{\text{vis}} S_w u_o - P_0 S_o \cong 0 \tag{11}$$

The solution to Eq. (11) is

$$u_o = \sqrt{\frac{P_0(1 - C_D)}{\rho_0 C_D} + \left[\frac{(1 - C_D)}{C_D}\frac{\kappa_{\text{vis}} S_w}{2\rho_0 S_o}\right]^2} - \frac{(1 - C_D)}{C_D}\frac{\kappa_{\text{vis}} S_w}{2\rho_0 S_o} \tag{12}$$

With u_o known, it is now possible to solve for resonator tuned resistance ($R_{\text{res}}/\rho_0 c_0$), defined as

$$R_{\text{res}}/\rho_0 c_0 \equiv P_0/\rho_0 c_0 \sigma u_o \tag{13}$$

Substituting Eq. (12) for u_o results in the following expression for resonator tuned resistance:

$$\frac{R_{\text{res}}}{\rho_0 c_0} = \sqrt{\left(\frac{1 - C_D}{C_D}\right)\left(\frac{P_0}{\rho_0 c_0^2 \sigma^2}\right) + \left(\frac{\kappa_{\text{vis}} S_w}{2\rho_0 c_0 \sigma S_o}\right)^2} + \frac{\kappa_{\text{vis}} S_w}{2\rho_0 c_0 \sigma S_o} \tag{14}$$

Linear resistance. At SPLs sufficiently low that nonlinear jetting losses are negligible, the resistive losses can be written as

$$R_L/\rho_0 c_0 = (1/\sigma)(\nu/c_0 d_o)(\tau/d_o)\left[K_{\text{ss}} + \sqrt{\left(\omega d_o^2/\nu\right)} K_{\text{ac}}\right] \tag{15}$$

In deriving Eq. (15), the parameter κ_{vis} was replaced by Eq. (10). Because at low SPL the resistance is independent of SPL and decoupled from reactance at all frequencies, Eq. (15) is not restricted to frequencies near resonance. In deriving Eq. (15), a factor four from the faceplate-wetted area S_w was absorbed into the parameters K_{ss} and K_{ac}.

It is of interest to compare the zero-frequency losses predicted by Eq. (15) to the steady-state losses predicted from fully developed laminar pipe flow[29,30]:

$$R_{\text{fd}}/\rho_0 c_0 = (32/\sigma)(\nu/c_0 d_o)(\tau/d_o) \tag{16}$$

Comparing these expressions yields $K_{\text{ss}} = 32$. Thus, it is reasonable to assume that $K_{\text{ss}} \to 32$ for resonators constructed such that $\tau/d_o \gg 1$. Combining Eqs. (14) and (15), the final expression for the resonator-tuned resistance is written as

$$R_{\text{res}}/\rho_0 c_0 = \sqrt{[(1 - C_D)/C_D]\left(P_0/\rho_0 c_0^2 \sigma^2\right) + (R_L/2\rho_0 c_0)^2} + R_L/2\rho_0 c_0 \tag{17}$$

Observe that at low SPL, $R_{\text{res}} \approx R_L$.

Reactance. The derivation starts from the following well-known lumped element (low SPL) expression for the reactance of a Helmholtz resonator:

$$X/\rho_0 c_0 = \omega d_e/\sigma c_0 - \cot(kL_c) \tag{18}$$

Ingard[4] derived the following approximate expression for the orifice inertial length parameter d_e:

$$d_e = \tau + \frac{0.85 d_o}{1 + 1.25\sqrt{\sigma}} \tag{19}$$

Motivated by the data shown in Fig. 2 and the suggestion by Ingard and Ising that nonlinear orifice jetting reduces orifice end correction, a simple reactance model is proposed by replacing d_e in Eq. (18) by an unknown inertial length parameter H:

$$X/\rho_0 c_0 = \omega H/\sigma c_0 - \cot(kL_c) \tag{20}$$

Here H is a function of SPL, frequency, and orifice geometry. Empirical solutions for H are presented in Sec. III.

III. Experimental Program

Resonator impedance is derived in terms of the four unknown parameters: K_{ss}, K_{ac}, C_D, and H. Low and high single-orfice SPL impedance tests were conducted to provide a database in order to generate empirical curve fits of these parameters. Table 1 summarizes the resonator plate thicknesses and orifice diameters tested. The values of τ and d_o, displayed in Table 1, result in a large range of values of τ/d_o.

Impedance measurements were conducted in a 5.08-cm-diam impedance tube constructed of 1.27-cm-thickness Lucite. The standing wave-pressure distributions within the tube were measured at several axial stations using 0.635-cm condenser microphones. These microphones were inserted into machined openings in the tube walls, which were filled with aluminum plugs when not in use. The facility was designed for impedance testing over a frequency range of approximately 20–3000 Hz. The tube was driven by a Community M4

compression driver capable of producing SPL in excess of 145 dB over most of the frequency range. Following the procedure recommended by Jones and Steide, data reduction was achieved using HP-VEE software using the two-microphone standing wave tube method.[31] At each test condition the axial positions of two microphones were swapped to average out response variations.

The test program consisted of measuring the impedance of the single-orifice resonator configurations described in Table 1 as a function of SPL and frequency. Very low-frequency resistive measurements were obtained by constructing the resonator backcavity walls with O-rings to achieve backcavity depths up to 177.8 cm. This is necessary to measure K_{ss} accurately.

A. Linear Parameters K_{ss} and K_{ac}

The linear resistances of resonators 1–6 of Table 1 are displayed in Fig. 3 as a function of frequency and orifice faceplate thickness. These measurements, recorded at SPL = 75 dB, were used in conjunction with Eq. (15) to determine the parameters K_{ss} and K_{ac}. Figure 4 displays the measured values of the viscous parameter K_{ss}.

The following curve fit of K_{ss} was derived:

$$K_{ss} = 13 + 10.23(\tau/d_o)^{-1.44} \tag{21}$$

The steady-state fully developed pipe-flow resistive loss coefficient of 32 is also plotted in Fig. 4. The measurements show that resonators constructed with very small values of τ/d_o have viscous scrubbing resistive losses that are much larger than fully developed pipe-flow resistive losses. These results are consistent with orifice entry and exit boundary-layer thicknesses that are less than the orifice radius. Conversely, resonators constructed with large ratios of τ/d_o have resistive losses substantially less than fully developed pipe flow. This was not expected. The derivation of the fully developed pipe-flow resistance model assumes that entry flow effects are negligible. For steady-state laminar flow pipe entry lengths as long as 150–300 pipe diameters have been measured.[29,30] These very long entry lengths suggest that three-dimensional effects ignored in the derivation of fully developed laminar resistance model can play an important role in explaining the data. For example, Fig. 5 is a sketch of an instantaneous laminar separation bubble formed near the orifice entry during inflow, which could explain the asymptotic behavior of $K_{ss} < 32$. Here, the orifice wetted area shear stresses in the laminar separation bubble would be opposite to the wall stresses on the remaining orifice wetted area, thereby reducing the net stress and hence K_{ss}.

Table 1 Geometry of single-orifice test resonators

Resonator ID	SPL regime	τ, cm	d_o, cm	τ/d_o	D_{cav}, cm	σ
1	Linear (75 dB)	0.159	0.318	0.5	5.08	0.0039
2		0.318	”	1	”	”
3		0.635	”	2	”	”
4		1.270	”	4	”	”
5		2.540	”	8	”	”
6		5.080	”	16	”	”
7	Nonlinear (120–140 dB)	0.159	0.635	0.25	5.08	0.0156
8		0.635	”	1	”	”
9		1.270	”	2	”	”
10		2.540	”	4	”	”
11		5.080	”	8	”	”

The corresponding values of K_{ac} are shown in Fig. 6. The following curve fit of K_{ac} was derived:

$$K_{ac} = 3 + 2.32(\tau/d_o)^{-1} \tag{22}$$

Figure 3, plotted in log–log scale, shows how well the curve fits of K_{ss} and K_{ac} defined by Eqs. (21) and (22) match the data over a wide frequency range for all of the resonator configurations. Attempts to match the thick faceplate data by forcing $K_{ss} = 32$ were unsuccessful.

B. Nonlinear Tuned Frequency F_{NL}

Although it is difficult to see, the reactance data displayed in Fig. 2 show the resonator tuned frequency to decrease with increasing SPL. The nonlinear tuned frequency F_{NL} is plotted in Fig. 7 as a function of faceplate thickness and SPL for resonators 7–11 of Table 1. The increase in frequency with SPL is consistent with the findings of other researchers. The nonlinear tuned frequency F_{NL} was correlated in terms of the ratio of two acoustic velocities. One is $\omega_L d_e$, which is based on resonator geometry. The other is $[P_{pk}/\rho_0]^{1/2}$, which characterizes the effect of SPL on orifice nonlinear jetting. The peak acoustic pressure is used instead of a rms value based on SPL

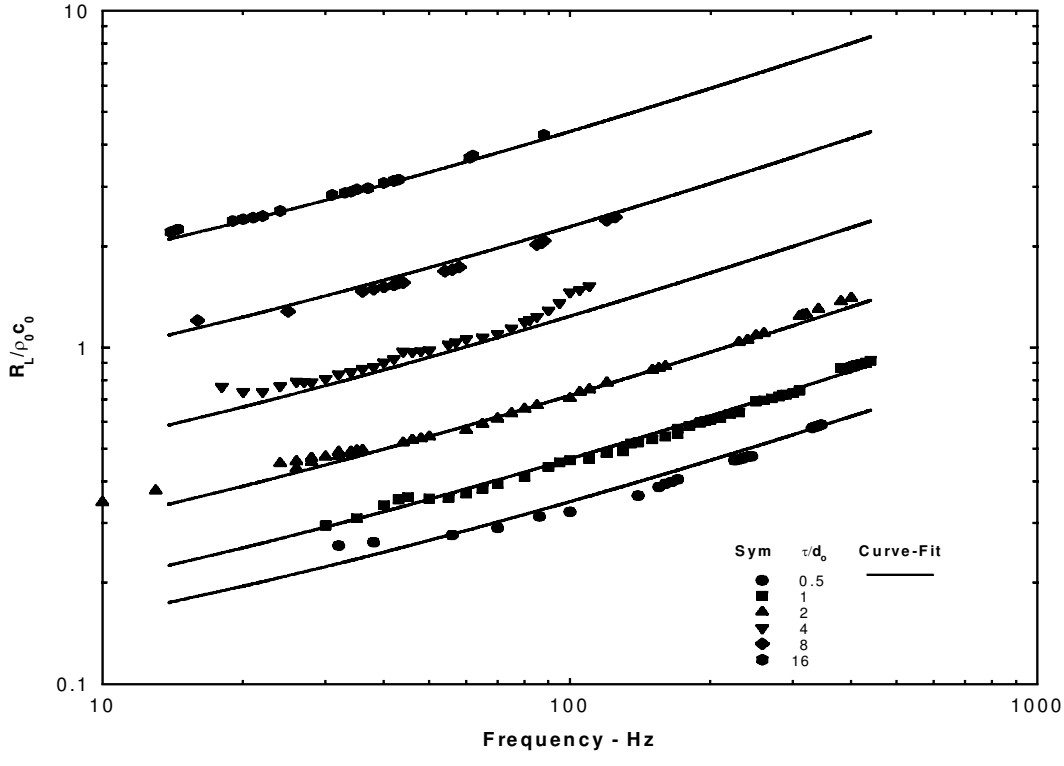

Fig. 3 Effect of faceplate thickness on linear resistance: d_o = 0.318 cm and SPL = 75 dB.

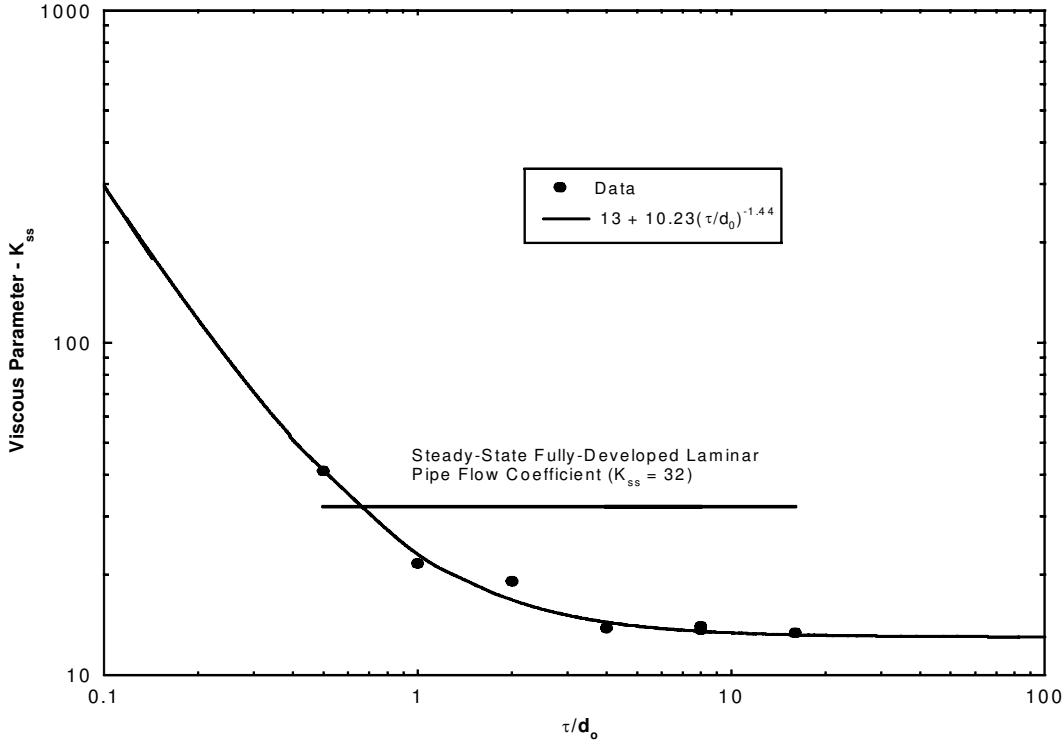

Fig. 4 Curve fit of parameter K_{ss}.

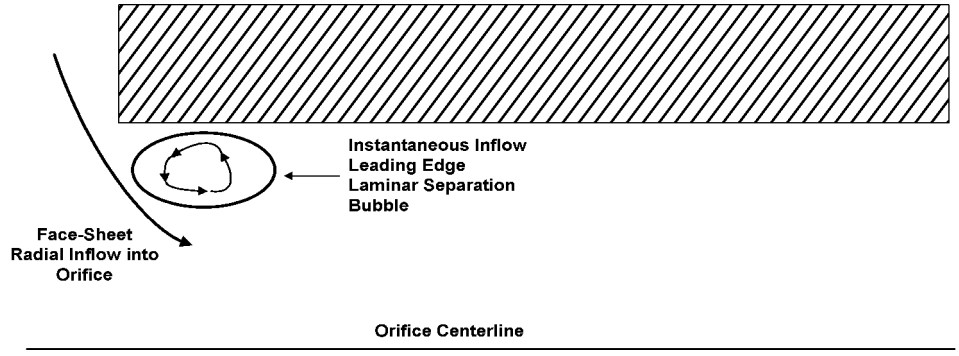

Fig. 5 Schematic of formation of laminar separation bubble during inflow.

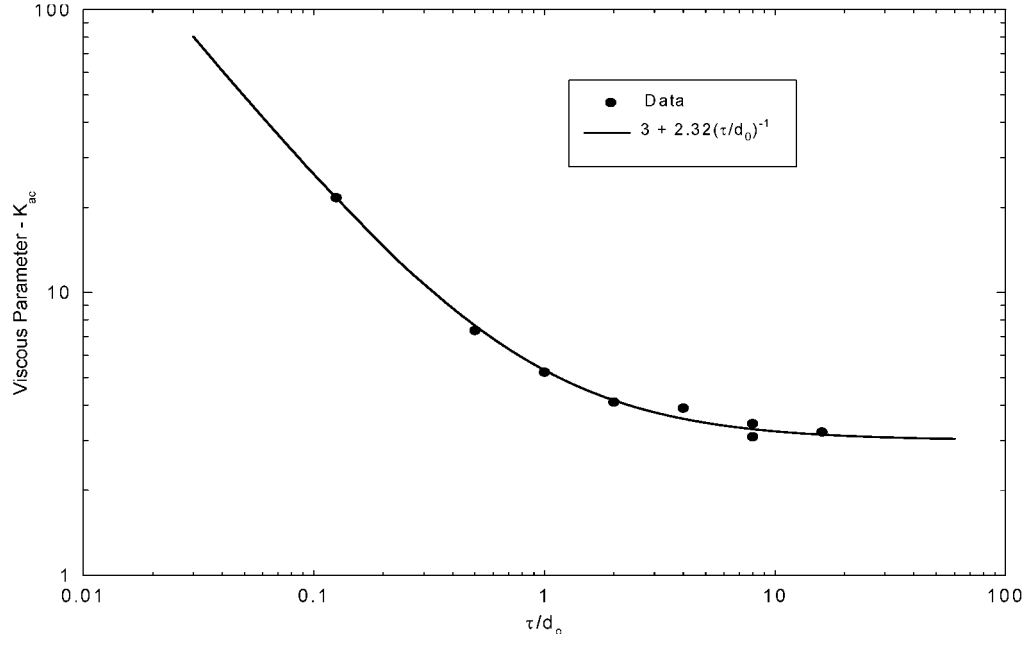

Fig. 6 Curve fit of parameter K_{ac}.

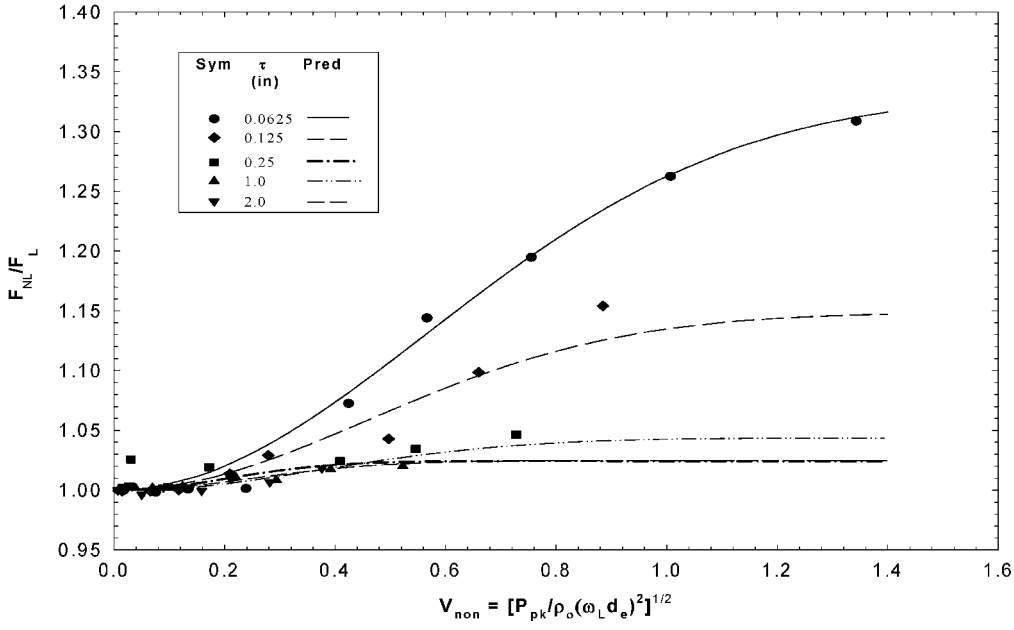

Fig. 7 Effect of faceplate thickness and sound-pressure amplitude on nonlinear tuned frequency F_{NL}: $d_o = 0.635$ cm, $L_c = 2.54$ cm, and $D_c = 5.08$ cm.

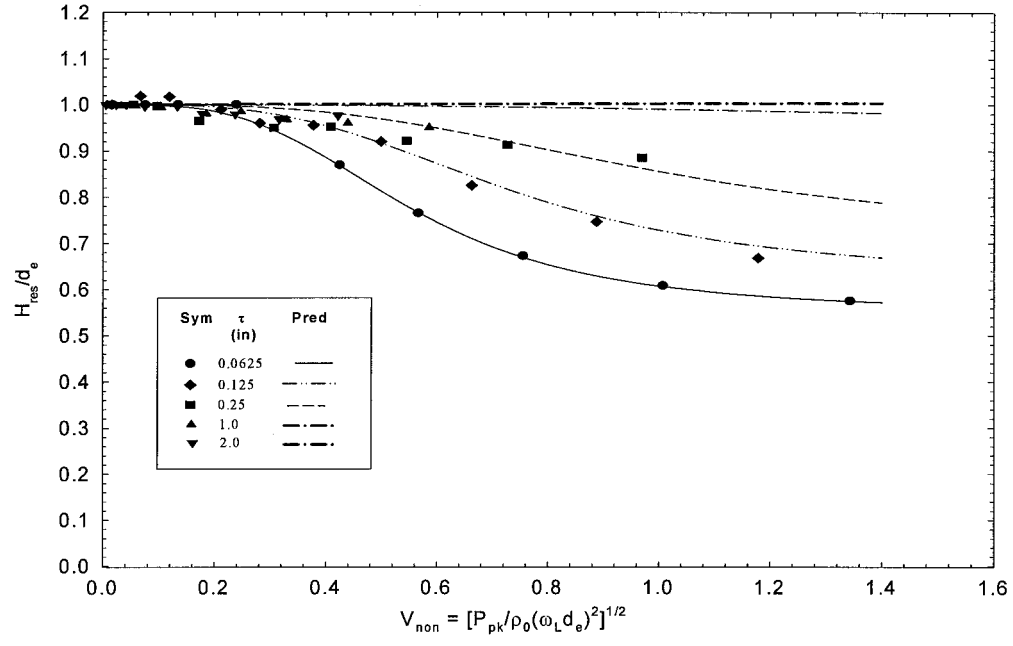

Fig. 8 Effect of faceplate thickness and sound-pressure amplitude on inertial parameter H_{res}: $d_o = 0.635$ cm, $L_c = 2.54$ cm, and $D_c = 5.08$ cm.

to be consistent with the peak values of Eq. (5). The ratio of these velocities defines the following nondimensional velocity parameter:

$$V_{\mathrm{non}} = \sqrt{P_{\mathrm{pk}} \big/ \rho_0 (\omega_L d_e)^2} \tag{23}$$

It will be shown in Sec. IV that V_{non} successfully predicts the impedance of a reasonably large number of resonator geometries reported in the open literature.

The data shown in Fig. 7 suggest that the effects of plate thickness are large when $\tau/d_o \leq 0.25$ and small when $\tau/d_o > 0.25$. The data further show that the effect of faceplate thichness becomes negligible when $\tau/d_o \geq 1$. The following curve fit of F_{NL} was derived:

$$F_{\mathrm{NL}}/F_L \approx 1 + a_F\left[1 - \exp\left(-b_F V_{\mathrm{non}}^2\right)\right]$$

$$a_F = 0.785 - 0.76\{1 - \exp[-3.63(\tau/d_o)]\}$$

$$b_F = 3.63(\tau/d_o)^{0.6} \tag{24}$$

C. Inertial Length Parameter H

The following procedure was used to model H. First, set $X = 0$ (resonance) in Eq. (20) and solve for H_{res}. With H_{res} determined, Eq. (20) is then solved for H/H_{res} as a function of frequency and SPL. At resonance the following expression for H_{res} was derived:

$$H_{\mathrm{res}} = \frac{\sigma c_0}{\omega_{\mathrm{NL}}(\mathrm{res})} \cot\left[\frac{\omega_{\mathrm{NL}}(\mathrm{res})\, L_{\mathrm{cav}}}{c_0}\right] \tag{25}$$

where $\omega_{\mathrm{NL}}(\mathrm{res}) \equiv 2\pi F_{\mathrm{NL}}(\mathrm{res})$ denotes the resonator nonlinear tuned (radian) frequency. Equation (25) was used to derive empirical values of H_{res}/d_e from impedance data. It is plotted in Fig. 8 in terms of the parameter V_{non} as a function of faceplate thickness and SPL for resonators 7–11 of Table 1.

The data show that at low SPL $H_{\mathrm{res}}/d_e \to 1$ and is insensitive to faceplate thickness. Conversely at high SPL H_{res}/d_e decreases with SPL and is sensitive to faceplate thickness. At high SPL and high τ/d_o, H_{res}/d_e approaches values between 0.5 and 0.6, which is

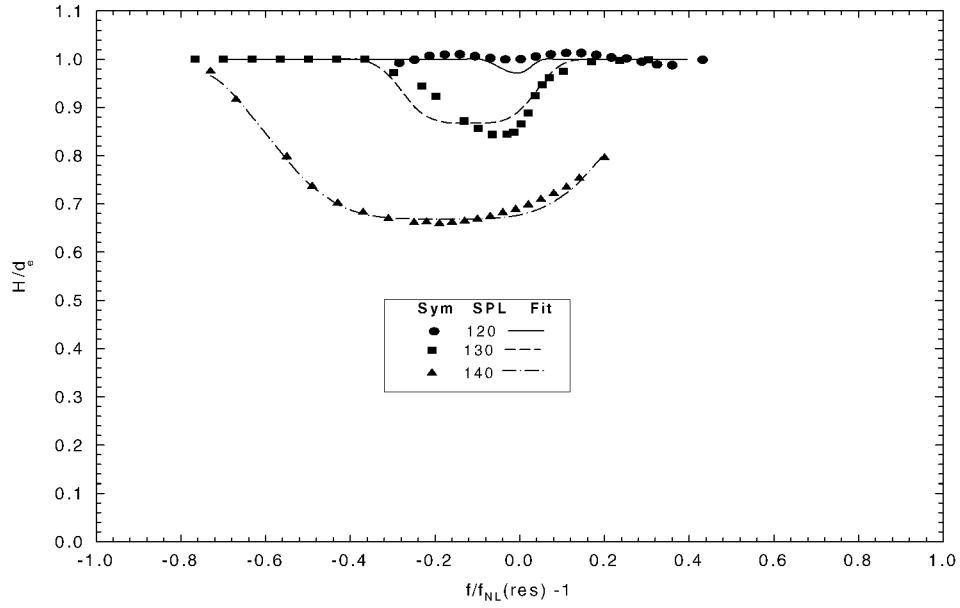

Fig. 9 Curve fit of inertial parameter H for thin face-sheet resonator: $\tau = 0.635$ cm, $L_c = 2.54$ cm, and $D_c = 5.08$ cm.

consistent with the measurements of Ingard and Ising.The following correlation of H_{res}/d_e in terms of SPL, sound frequency, and resonator geometry was derived:

$$\frac{H_{\text{res}}}{d_e} \approx \frac{1 + a_H V_{\text{non}}^{m_H}}{1 + b_H V_{\text{non}}^{m_H}}, \qquad a_H = 0.725\left(\frac{\tau}{d_o}\right)^{-1.227}$$

$$b_H = 1.02\left(\frac{\tau}{d_o}\right)^{-1.411}, \qquad m_H = 3.42e^{-0.117(\tau/d_o)} \tag{26}$$

The effect of frequency on H/d_e is plotted in Fig. 9 for resonator configuration 7 of Table 1. The data suggest that $H/d_e \to 1$ for frequencies well below and above resonance.

Curve fits similar to Fig. 9 were obtained for resonator configurations 8–11. The following rather complicated curve fit of H/d_e was derived:

$$H/d_e = 1 - (1 - H_{\text{res}}/d_e)\exp\left[-m_H\left(f\,/\,f_{\text{NL}} - 1 - f_o^*\right)^4\right] \tag{27}$$

where

$$m_H = \frac{\alpha_H}{V_{\text{non}}^{\beta_H}} + \kappa_H, \qquad \alpha_H = 0.011 + 2.086\left(\frac{\tau}{d_o}\right)$$

$$\beta_H = \frac{0.0325}{(\tau/d_o)^{3.7}} + 3.4$$

$$\kappa_H = 13.06\left\{1 - \exp\left[-64.9\left(\frac{\tau}{d_o}\right)^{4.365}\right]\right\}$$

$$f_o^* = \frac{(1.34/V_{\text{non}})(\tau/d_o)}{1 + 18.81(\tau/d_o)} + 0.264\left\{1 - \exp\left[-4.49\left(\frac{\tau}{d_o}\right)\right]\right\} - 0.436 \tag{28}$$

D. Acoustic Discharge Coefficient Parameter C_D

The effects of SPL, frequency, and resonator geometry on C_D were determined from experimental data using Eq. (17). The effect of faceplate thickness and SPL on C_{Dres} at resonance, displayed in Fig. 10, was calculated in terms of the nondimensional parameter $V_{\text{non}} = [P_{\text{pk}}/\rho(\omega_L d_e)^2]^{1/2}$.

Observe that $C_{\text{Dres}} \to 1$ as SPL $\to 0$. At high SPLs, $C_{\text{Dres}} \to 0.64$ and is almost independent of orifice geometry. This value is quite close to the steady-state values of approximately 0.6 measured in thin, sharp-edges orifices.[28]

It is of interest to determine at high SPL the orifice-based Reynolds number based on orifice particle velocity and orifice diameter ($R_e \equiv u_o d_o/\nu$). Selecting SPL = 140 dB ($P_0 = 2000$ dynes/cm^2) and assuming that viscous resistive losses are negligible, the orifice velocity u_o can be estimated from Eqs. (13) and (14) as

$$u_o = \frac{P_D}{\rho c \sigma R_{\text{res}}} \cong \frac{P_D}{\rho c \sigma \sqrt{[(1 - C_D)/C_D]\left(P_D\,/\,\rho c^2 \sigma^2\right)}}$$

$$= \sqrt{\left(\frac{C_D}{1 - C_D}\right)\frac{P_D}{\rho}} \tag{29}$$

From Fig. 10 it is reasonable to assume $C_D \cong 0.64$. This yields $R_e \cong 7.3 \times 10^3$, which is sufficiently large to support the assumption that viscous effects are negligible.

The following curve fit to C_{Dres} was derived:

$$C_{\text{Dres}} = \frac{1 + a_{\text{CDres}} V_{\text{non}}^2}{1 + b_{\text{CDres}} V_{\text{non}}^2}$$

$$a_{\text{CDres}} = \frac{1 + 110.5\exp[0.647(\tau/d_o)]}{1 + 0.109\exp[0.647(\tau/d_o)]}$$

$$b_{\text{CDres}} = \frac{1 + 168.5\exp[0.647(\tau/d_o)]}{1 + 0.109\exp[0.647(\tau/d_o)]} \tag{30}$$

The effect of frequency on the ratio $C_{\text{D}}/C_{\text{Dres}}$ is plotted in Fig. 11 for the thin face-sheet resonator,$\tau/d_o = 0.0625$. Curve fits similar to Fig. 11 were obtained for resonator configurations 8–11 of Table 1.

The rather complicated curve fit of the discharge coefficient frequency data was derived:

$$C_D = \frac{C_{\text{Dres}} + a_{\text{CD}} f_{\text{non}}^2}{1 + b_{\text{CD}} f_{\text{non}}^2 + a_{\text{CD}} f_{\text{non}}^2}, \qquad f_{\text{non}} \equiv \frac{f_{\text{NL}}}{f} - 1 \tag{31}$$

where

$$a_{\text{cd}} = a_{1\text{CD}} + a_{2\text{CD}}\exp(-a_{3\text{CD}} V_{\text{non}})$$

$$a_{1\text{CD}} = 18.81\frac{\tau}{d_o} - 57.11\sqrt{\frac{\tau}{d_o}}\left[1 - \exp\left(-0.18\frac{\tau}{d_o}\right)\right]$$

$$a_{2\text{CD}} = \exp\left\{\frac{33.5(\tau/d_o) - 78(\tau/d_o)^2 + 131(\tau/d_o)^3 + 917(\tau/d_o)^4}{1 + 148(\tau/d_o)^4}\right\}$$

$$a_{3\text{CD}} = 43.2\frac{\tau}{d_o} - 147.1\sqrt{\frac{\tau}{d_o}}\left[1 - \exp\left(-0.19\frac{\tau}{d_o}\right)\right] \tag{32}$$

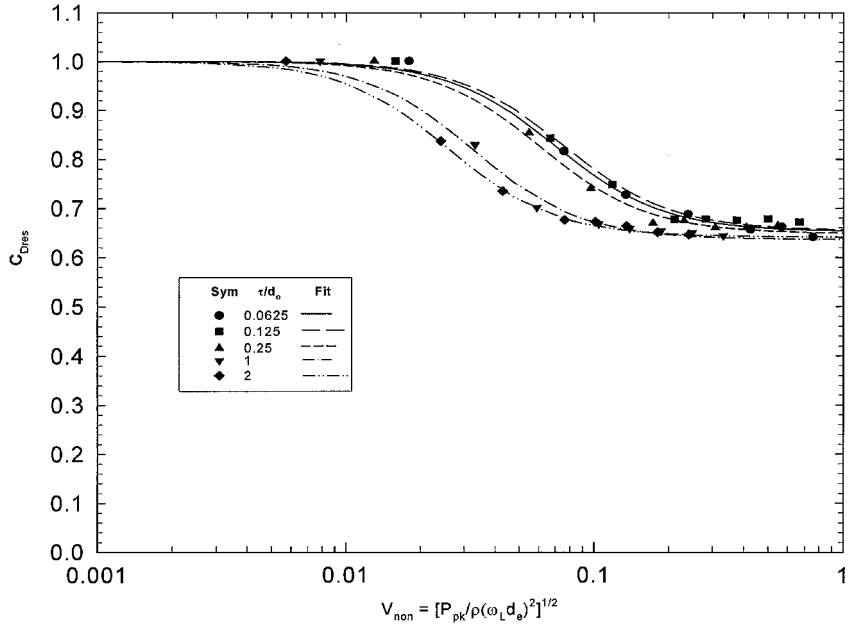

Fig. 10 Effect of faceplate thickness and sound-pressure amplitude on parameter C_{Dres}: $d_o = 0.635$ cm, $L_c = 2.54$ cm, and $D_c = 5.08$ cm.

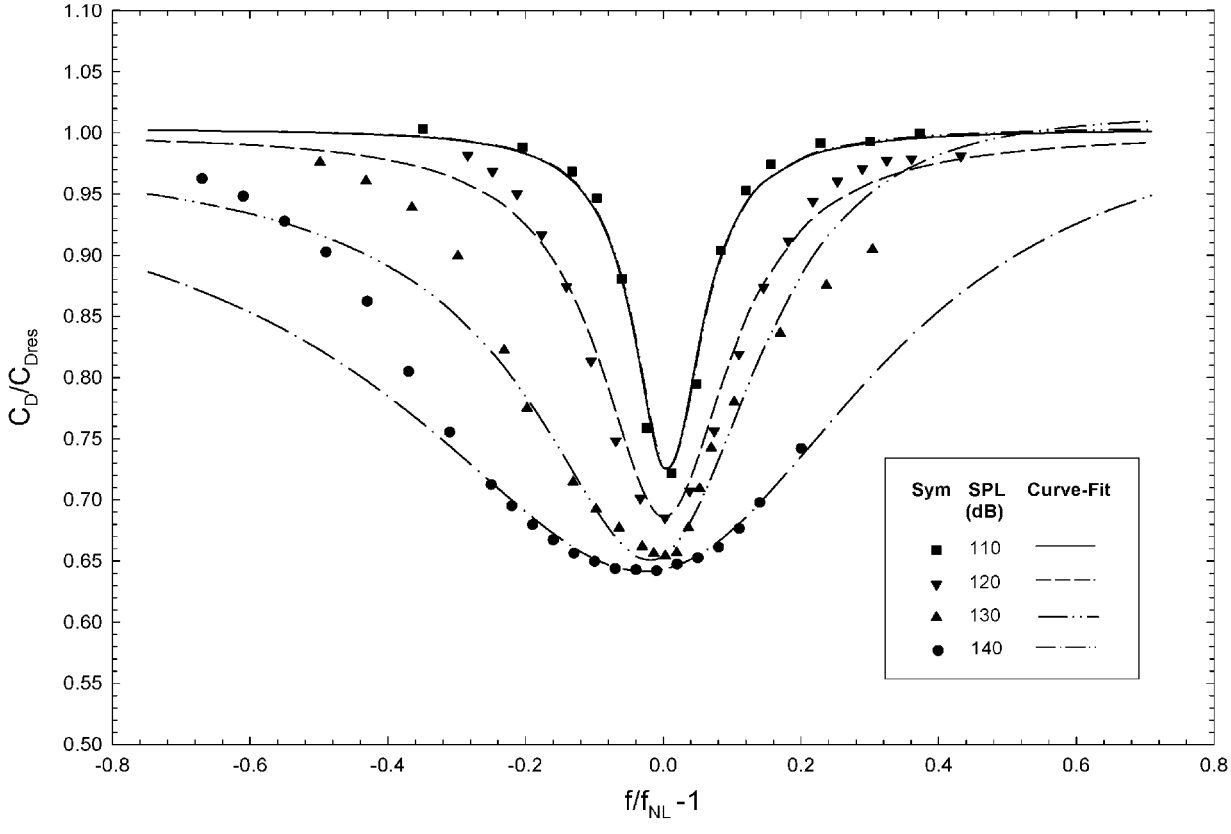

Fig. 11 Curve fit of effect of frequency on discharge coefficient parameter for thin face-sheet resonator: $\tau = 0.159$ cm, $d_o = 0.635$ cm, $L_c = 2.54$ cm, and $D_c = 5.08$ cm.

$$b_{\mathrm{cd}} = \frac{b_{1\mathrm{CD}} + b_{2\mathrm{CD}} V_{\mathrm{non}}}{1 + b_{3\mathrm{CD}} V_{\mathrm{non}}}, \qquad b_{1\mathrm{CD}} = \frac{-3.44 - 0.182(\tau/d_o)}{1 + 0.342(\tau/d_o)}$$

$$b_{2\mathrm{CD}} = \frac{18.23 + 1.33(\tau/d_o)}{1 + 0.151(\tau/d_o)}, \qquad b_{3\mathrm{CD}} = \frac{38}{1 + 1.3 * 10^{-7}(\tau/d_o)^2} \tag{33}$$

Inserting the preceding empirical curve fits to the parameters K_{ss}, K_{ac}, F_{NL}, H, and C_D into the following equation results in the final generalized expression for resonator resistance as a function of SPL, resonator geometry, and frequency:

$$R/\rho_0 c_0 = \sqrt{[(1 - C_D)/C_D]\left(P_D \big/ \rho_0 c_0^2 \sigma_o^2\right) + (R_L/2\rho_0 c_0)^2} + R_L/2\rho_0 c_0 \tag{34}$$

Finally, resonator reactance is defined by Eq. (20).

IV. Model Validation

Model validation is divided into two parts. The first compares predicted and measured impedance of resonators 7–10 of Table 1 and also compares predicted impedance to unpublished multiple orifice resonator impedance data. Because the curve-fit expressions

derived for the parameters K_{ss}, K_{ac}, F_{NL}, H, and C_D were based on the impedance measurements of these resonators, it is reasonable to expect good agreement between model predicted and measured impedance. This will be shown to be true in the following section. The second part compares predicted impedance to measurements published in the open literature.

A. Part 1: Predicted and Measured Impedance of Table 1 Resonators

Figures 12a–12c compare predicted vs measured impedance for resonators 7, 9, and 11 corresponding to the smallest, midsize, and largest face-sheet thicknesses of 0.159, 0.635, and 5.08 cm, respectively. The comparison shows that the simple one-dimensional model fairly accurately predicted resonator resistance and reactance over the entire measured frequency and SPL range. The remaining plate thicknesses of 0.318, 1.27, and 2.54 cm (not shown) were also fairly accurately predicted.

The measured values of K_{ss} and K_{ac}, defined by Eqs. (21) and (22), were used to predict the viscous resistive losses of three multiple orifice resonators constructed with 1, 4, and 64 orifices at SPL = 80 dB. The orifices were constructed so that both orifice percent open area and orifice-to-orifice spacing were held constant at $\sigma = 0.0352$ and $S_N/d_N = 2$, respectively. With σ constant the following relationship holds between orifice diameter and orifice number:

$$d_N = d_o/\sqrt{N} \tag{35}$$

The correlation shown in Fig. 13 was used to predict the effect of orifice number on orifice end correction and hence resonator

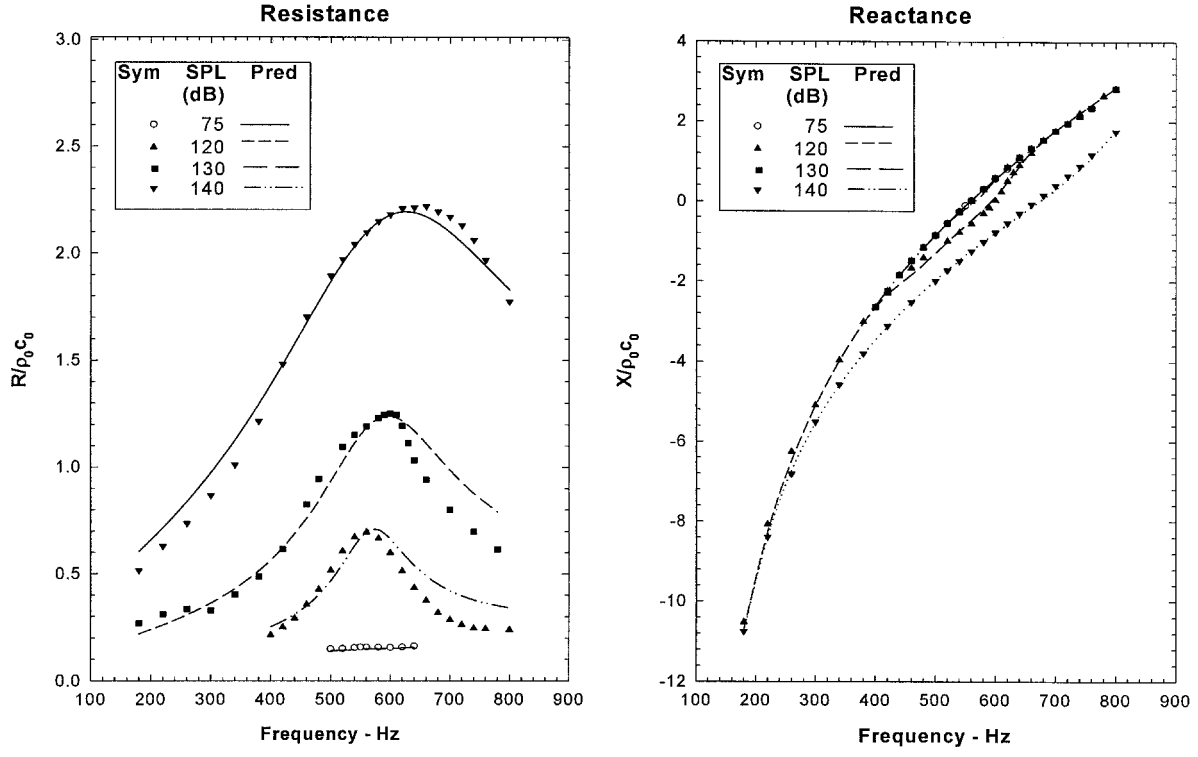

Fig. 12a Predicted and measured impedance of thin face-sheet resonator: $\tau = 0.159$ cm, $d_o = 0.635$ cm, $L_c = 2.54$ cm, and $D_c = 5.08$ cm.

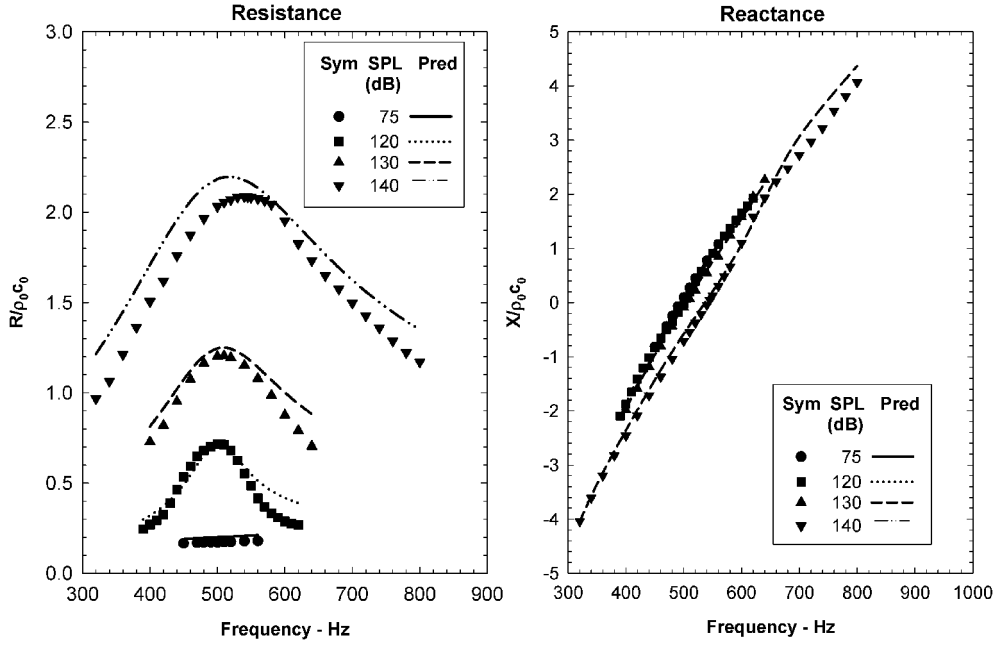

Fig. 12b Predicted and measured impedance of thin face-sheet resonator: $\tau = 0.635$ cm, $d_o = 0.635$ cm, $L_c = 2.54$ cm, and $D_c = 5.08$ cm.

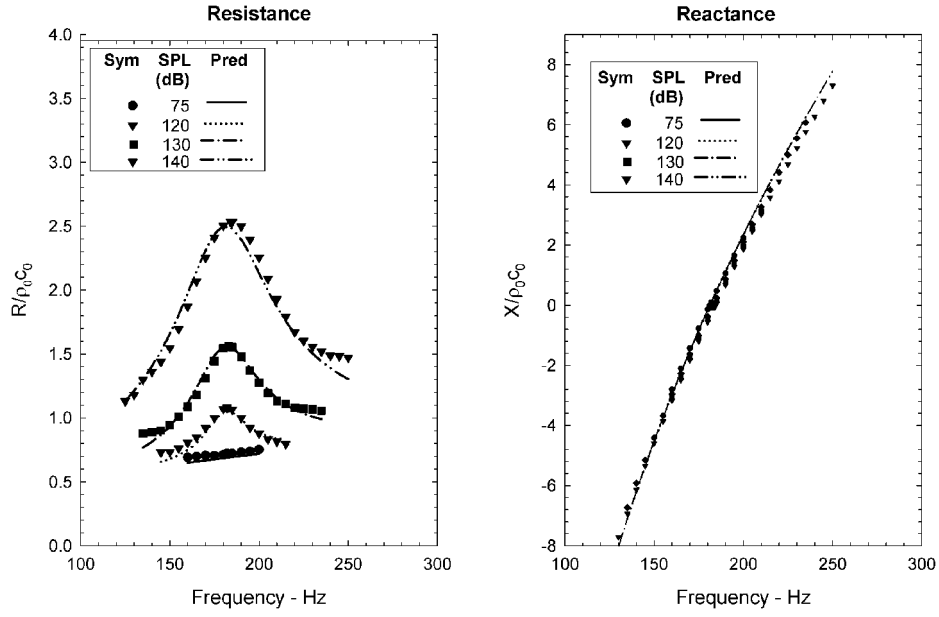

Fig. 12c Predicted and measured impedance of thick face-sheet resonator: $\tau = 5.08$ cm, $d_o = 0.635$ cm, $L_c = 2.54$ cm, and $D_c = 5.08$ cm.

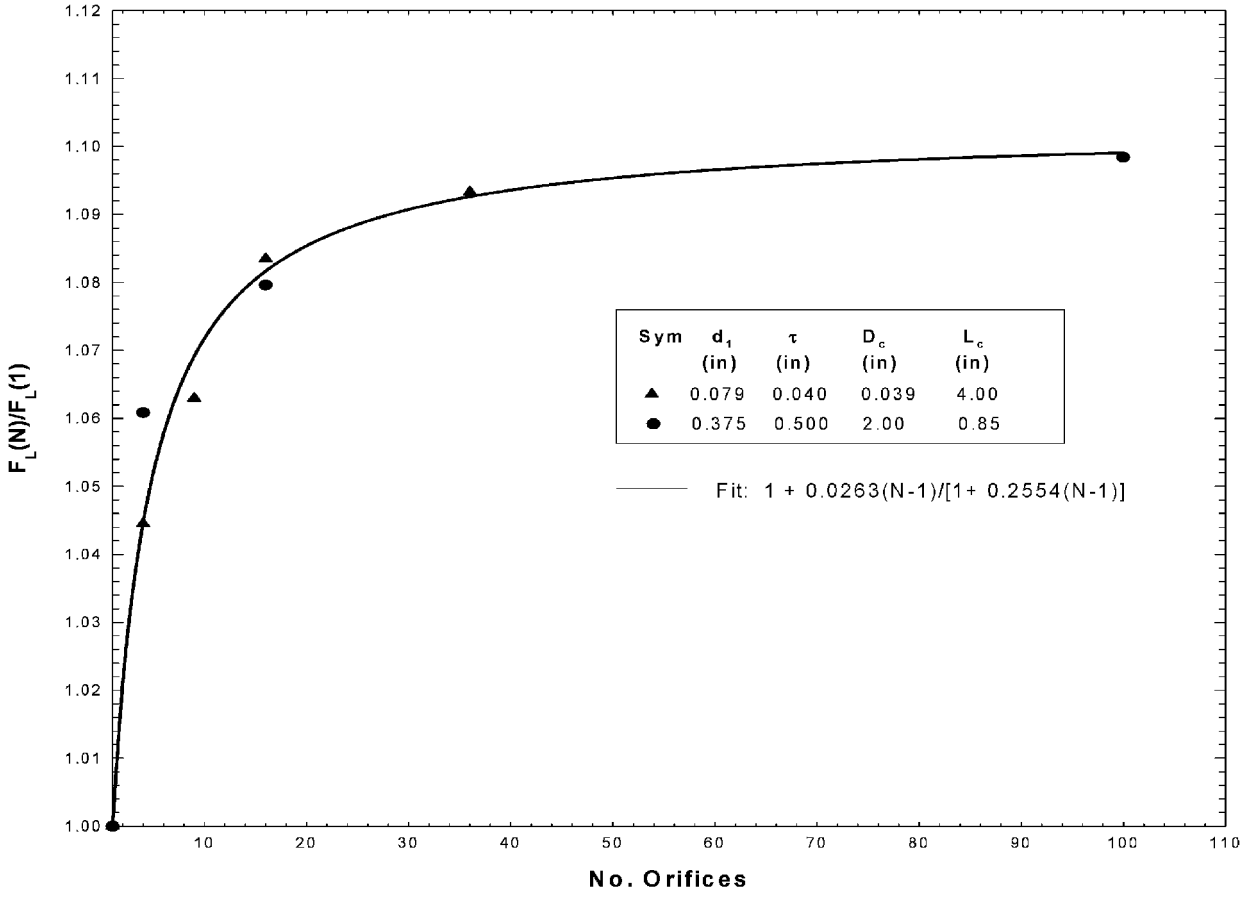

Fig. 13 Curve fit of effect of multiple orifices on resonator tuned frequency.

reactance. By normalizing the thin and thick orifice thickness data as shown in Fig. 13, the following curve fit that is independent or almost independent of orifice plate thickkness was derived:

$$\frac{F_L(N)}{F_L(1)} \simeq 1 + \frac{0.0263(N-1)}{1 + 0.2554(N-1)} \tag{36}$$

The low SPL resistance of resonators constructed with multiple orifices was calculated from Eqs. (15), (21), (22), and (35), and the corresponding reactance was calculated from Eqs. (20), (35), and (36). Figures 14 and 15 show that the model predicted impedance for the thin and thick face-sheet resonator configurations shown in Tables 2 and 3 compare favorably with measurements. Because the model does not account for the effects of orifice spacing, this good agreement suggests that resonator impedance is insensitive to orifice spacing when $S_N/d_N \geq 2$.

B. Part 2: Predicted and Measured Impedance Published in Open Literature

The resonator model was used to predict the resistive losses of resonators published in the open literature by Thurston and

Table 2 Geometry of thin faceplate resonators: $L_c = 10.16$ cm, $\sigma = 0.041$, $\tau = 0.102$ cm

N	d_N, cm	S_N, cm	S_N/d_N
1	1.029	0	NA
4	0.514	1.043	2.03
16	0.257	0.488	1.9
100	0.103	0.196	1.9

Table 3 Geometry of thick faceplate resonators: $L_c = 2.159$ cm, $\sigma = 0.035$, $\tau = 1.27$ cm

N	d_N, cm	S_N, cm	S_N/d_N
1	0.9500	1.9000	NA
4	0.4750	0.9500	2.00
9	0.3170	0.6340	2.00
16	0.2380	0.4760	2.00
64	0.1190	0.2380	2.00

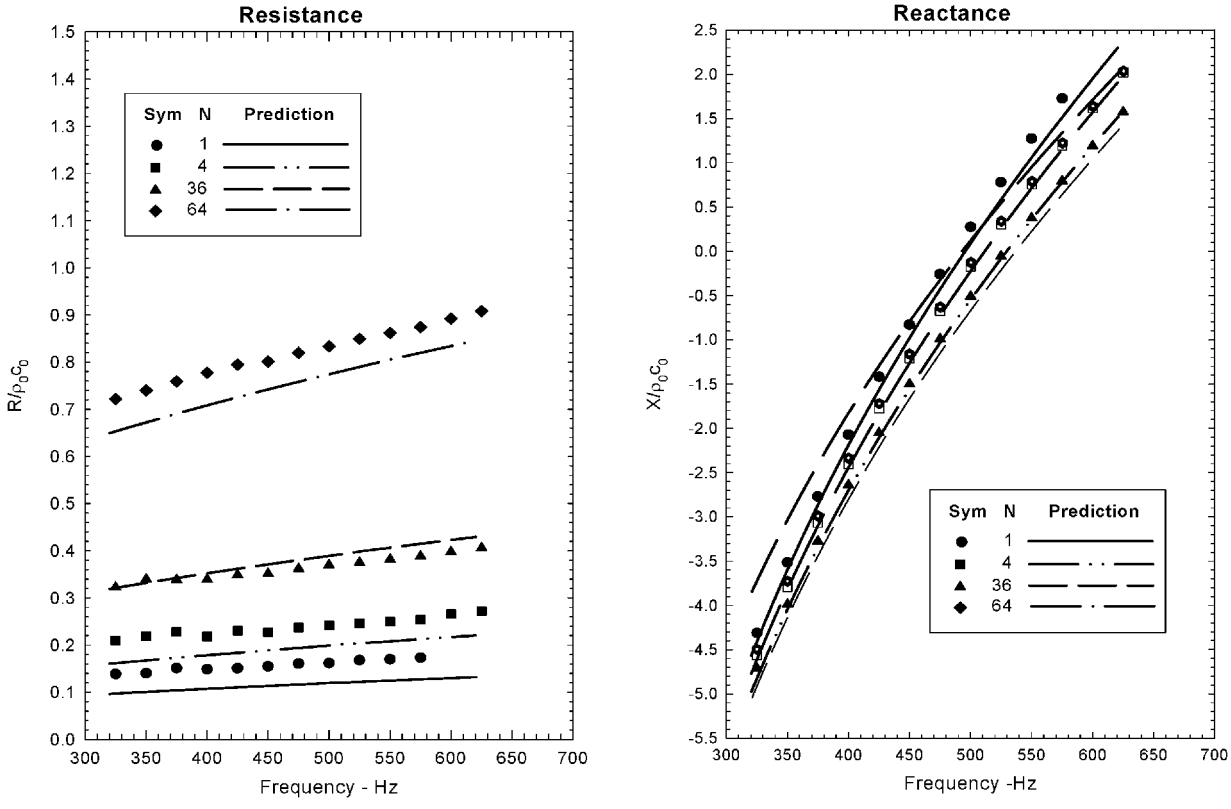

Fig. 14 Predicted and measured impedance of multiple-orifice resonators: SPL = 80 dB, $\tau = 1.27$ cm, $D_c = 5.08$ cm, $L_c = 2.16$ cm, $\sigma = 0.0352$, and $S_N/d_o = 2$.

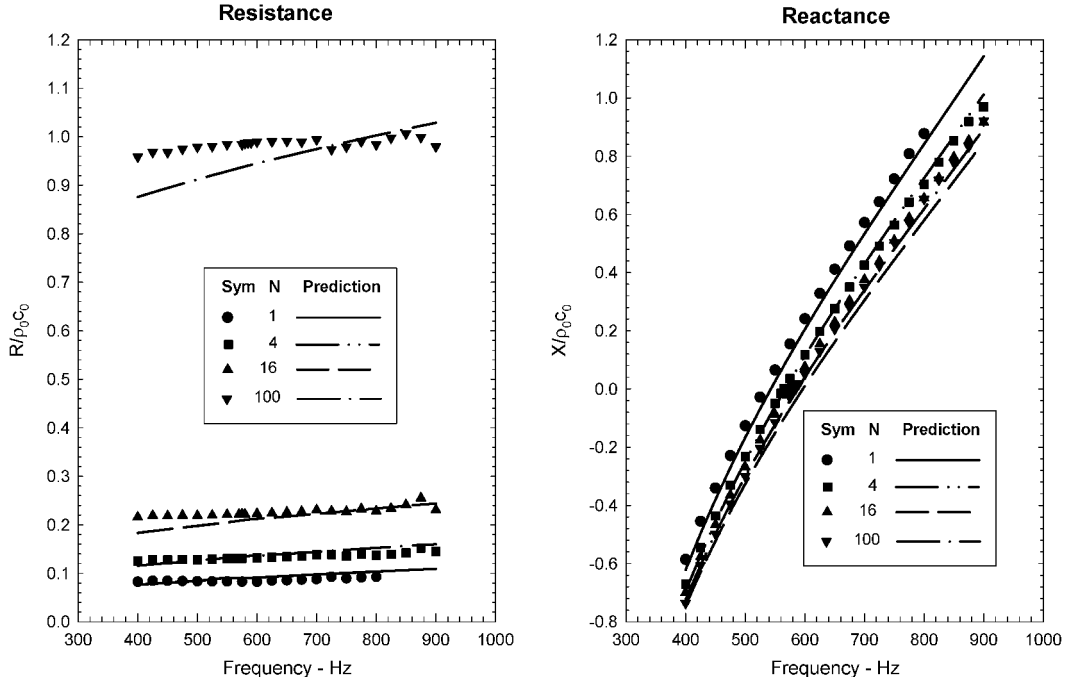

Fig. 15 Predicted and measured impedance of multiple-orifice resonators: SPL = 80 dB, $\tau = 0.102$ cm, $D_c = 0.991$ cm, $L_c = 10.16$ cm, and $S_N/d_N = 2$.

Martin,[32] Bies and Wilson,[33] Melling,[6] and Ingard and Ising.[13] The measured values of K_{ss} and K_{ac} were used to predict the viscous resistive losses of four resonators measured in water by Thurston. The predicted and measured resistance of the four resonators is shown in Fig. 16. The agreement is remarkable because the empirical curve fits of the parameters K_{ss} and K_{ac} were extended well outside their measured range. The good comparison between water and air validates the assumptions used to derive the continuity and momentum equations: the acoustic impedance of Helmholtz resonators is governed by unsteady, incompressible fluid behavior.

Bies and Wilson[33] measured the resistance of a resonator constructed with a single orifice of diameter $d_o = 3.5$ in., plate thickness $\tau = 2.87$ cm, and cavity diameter $D_c = 44.45$ cm. Although Fig. 17 indicates that the model underpredicts the measured resistance, it does, nonetheless, show good qualitative agreement between predicted and measured resistance at both low and high SPL. This is important because Bies and Wilson measured very hot cavity temperatures at high SPL, reaching a maximum of 133°C at SPL = 170 dB. Incorporating the temperature increase in the fluid viscosity, density, and speed of sound resulted in the good qualitative agreement shown.

The measurements of Melling were used to further validate the model. Melling measured the impedance of a series of resonators constructed with multiple orifices backed by a cavity. Figure 18

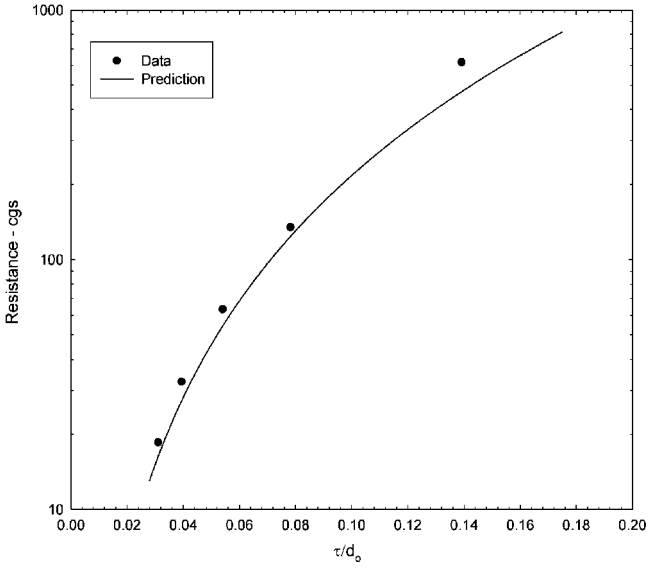

Fig. 16 Measured and predicted linear resistance of Thurston and Martin[32] of small orifices immersed in water: $\tau = 0.014$ cm and $L_c = 1.0$ cm.

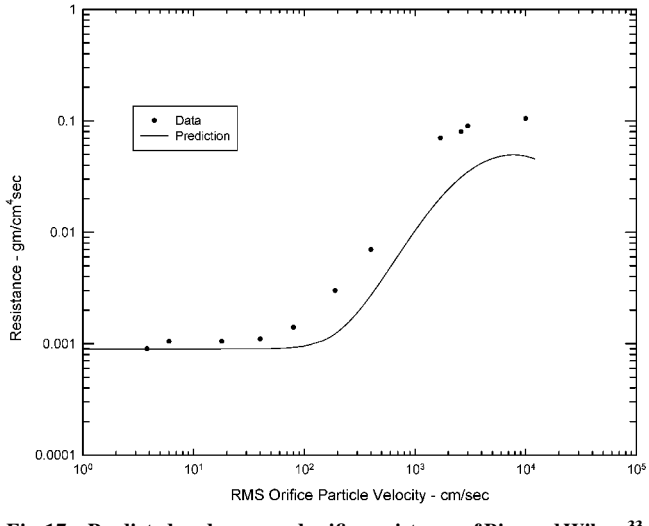

Fig. 17 Predicted and measured orifice resistance of Bies and Wilson[33] data: $d_o = 3.5$-cm, $\tau = 2.87$ cm, and $D_c = 44.45$ cm.

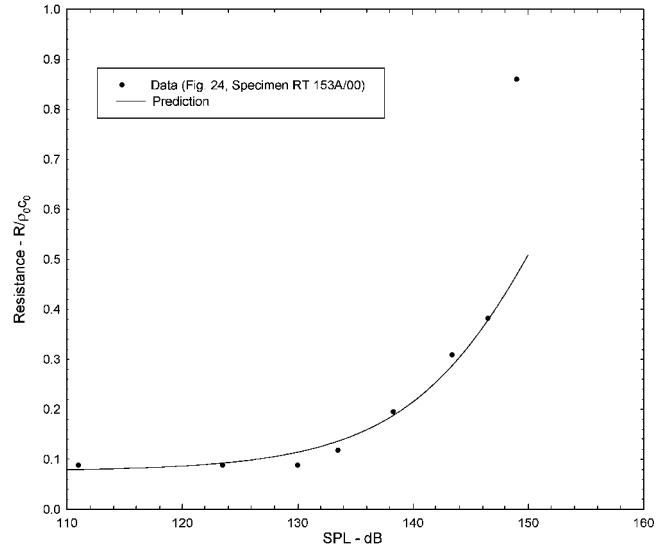

Fig. 18 Predicted and measured resistance measurements by Melling[6]: $d_o = 0.127$ cm, $\tau = 0.056$ cm, $\sigma = 0.075$, $L_c = 2.54$ cm, and $S/d_o = 3.46$.

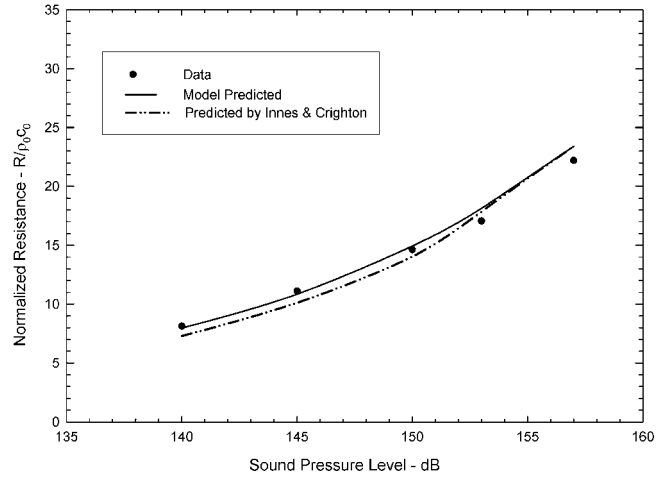

Fig. 19 Model and Ingard and Ising[13] measured resistance: $d_o = 07$ cm, $\tau = 0.01$ cm, $D_c = 9.5$ cm, and $L_c = 7.5$ cm.

shows that the model predicted the linear and nonlinear resistance of a resonator constructed with an orifice diameter $d_o = 0.05$ in., plate thickness $\tau = 0.056$ cm, percent open area $\sigma = 0.075$, cavity depth $L_c = 2.54$ cm, and orifice spacing $S/d_o = 3.46$. As shown, the model again predicted quite accurately the resonator linear and non-linear resistance.

Figure 19 compares model-predicted resistance (near resonance) with the hot-wire resistance measurements conducted by Ingard and Ising[13] on a resonator constructed with an orifice diameter of 0.7 cm, faceplate thickness of 0.1 cm, cavity depth of 7 cm, and cavity diameter of 9.5 cm. As shown, the model accurately predicted resonator resistance as well as a theoretical estimate of resonator resistance, valid at high SPLs, derived by Innes and Crighton.[34]

V. Conclusions

Impedance measurements of resonators were correlated in terms of the nondimensional velocity $[P_{pk}/\rho_0(\omega_L d_e)^2]^{1/2}$. The acoustic velocities $\omega_L d_e$ and $[P_{pk}/\rho_0]^{1/2}$ characterize the effects of resonator geometry and SPL on resonator impedance, respectively. The model successful prediction of the measured impedance of a relatively large number of resonators constructed with single and multiple orifices warrants its use in preliminary design applications. This successful agreement was achieved providing multiple-orifice spacing $S_N/d_N \geq 2$.

Test data have shown that at very low frequencies resonators constructed with thin faceplates relative to orifice diameter have

viscous resistive losses that are larger than predicted from orifice fully developed laminar boundary-layer theory. These results are consistent with orifice entry boundary-layer thicknesses that are smaller than orifice diameter. Test data also show that resonators constructed with thick faceplates relative to orifice diameter have resistive losses less than those predicted from fully developed laminar boundary-layer theory. This was not expected and is not understood, although it is suggested that inlet laminar separation bubbles may play an important role in explaining the test data. It is recognized that resonator viscous resistive losses are difficult to measure accurately because they require the extrapolation of impedance tube data to zero or very low frequencies. Consideration should be given, therefore, to the use of hot wires to measure orifice acoustic velocity and inlet/outlet boundary-layer thicknesses. These data would provide a direct measurement of resonator impedance. Further, the data could also be used to calibrate numerical codes.

Acknowledgment

The authors acknowledge the insightful and important contributions made by Gerald Bielak of the Boeing Commercial Aircraft Co.

References

[1]Rayleigh, Lord, *Theory of Sound*, Dover, New York, 1945, pp. 16, 17.

[2]Junger, M. C., "Helmholtz Resonators in Load-Bearing Walls," *Noise Control Engineering*, Vol. 4, No. 1, 1975, pp. 17–25.

[3]Crandall, I. B., *Theory of Vibration Systems and Sound*, D. Van Nostrand, New York, 1927.

[4]Ingard, U., "On the Theory and Design of Acoustical Resonators," *Journal of the Acoustical Society of America*, Vol. 25, 1953, pp. 1037–1062.

[5]Sivian, L. J., "Acoustic Impedance of Small Orifices," *Journal of the Acoustical Society of America*, Vol. 7, Oct. 1935, pp. 94–101.

[6]Melling, T. H., "The Acoustic lmpedance of Perforates at Medium and High Sound Pressure Levels," *Journal of Sound and Vibration*, Vol. 29, No. 1, 1973, pp. 1–65.

[7]Sirignano, W. A., "Non Linearita dei Risonatori di Helmholtz," *Aerotecnica Missili E Spazio*, Vol. 4, 1972, pp. 256–265.

[8]Zinn, B. T., "A Theoretical Study of Non-Linear Damping by Helmholtz Resonators," *Journal of Sound and Vibration*, Vol. 13, No. 3, 1970, pp. 347–356.

[9]Hersh, A. S., and Rogers, T., "Fluid Mechanical Model of the Acoustic Impedance of Small Orifices," NASA CR-2682, May 1976.

[10]Hersh, A. S., and Walker, B., "Effect of Grazing Flow on the Impedance of Helmholtz Resonators Consisting of Single and Clustered Orifices," NASA CR3177, Aug. 1979.

[11]Hersh, A. S., and Walker, B. E., "Non-Linear Acoustic Behavior of Helmholtz Resonators," U.S. Air Force Phillips Lab., Rept. PL-TR-91-3077, Edwards AFB, CA, Dec. 1991.

[12]Ingard, U., and Labate, S., "Acoustic Circulation Effects and the Non-Linear Impedance of Orifices," *Journal of the Acoustical Society of America*, Vol. 22, March 1950, pp. 211–219.

[13]Ingard, U., and Ising, H., "Acoustic Non-Linearity of an Orifice," *Journal of the Acoustical Society of America*, Vol. 42, No. 1, 1967, pp. 6–17.

[14]Yang, I. J., and Cummings, A., "A Time Domain Solution for the Attenuation, at High Amplitudes, of Perforated Tube Silencers and Comparison with Experiment," *Journal of Sound and Vibration*, Vol. 122, No. 2, 1988, pp. 243–259.

[15]Cummings, A., "Acoustic Non-Linearities and Power Losses at Orifices," AIAA Paper 83-0739, April 1983.

[16]Jing, X., and Sun, X., "Numerical Simulation on the Non-Linear Acoustic Properties of an Orifice," AIAA Paper 99-1878, May 1999.

[17]Jing, X., and Sun, X., "Discrete Vortex Simulation on the Acoustic Nonlinearity of an Orifice," *AIAA Journal*, Vol. 38, No. 9, 2000, pp. 1565–1572.

[18]Jing, X., and Sun, X., "Sound Excited Flow and Acoustic Non-Linearity of an Orifice," *Physics of Fluids*, Vol. 14, Jan. 2002, pp. 268–276.

[19]Cummings, A., and Eversman, E., "Transient and Multiple Frequency Sound Transmission Through Perforated Elastic Screens," *Journal of the Acoustical Society of America*, Vol. 79, No. 4, 1986, pp. 942–951.

[20]Durrieu, P., Ajello, R., Boot, R., Auregan, Y., Hirschberg, A., and Peters, M. C. A. M., "Quasisteady Aero-Acoustic Response of Orifices," *Journal of the Acoustical Society of America*, Vol. 110, No. 4, 2000, pp. 1859–1872.

[21]Peters, M. C. A. M., and Hirschberg, A., "Acoustically Induced Periodic Vortex Shedding at Sharp-Edged Open Channel Ends: Simple Vortex Models," *Journal of Sound and Vibration*, Vol. 161, 1993, pp. 281–299.

[22]Verge, M. P., Fable, B., Mahu, W. E. A., Hirschberg, A., Van Hassel, R. R., Wijnands, A. P. J., DeVries, J. J., and Hogendoorn, C. J., "Jet Formation and Jet Velocity in a Flue Organ Pipe," *Journal of the Acoustical Society of America*, Vol. 95, 1994, pp. 110–1132.

[23]Bruggeman, J. C., Hirschberg, A., Van Dongen, M. E. H., and Wijnands, A., "Self-Sustained Aero-Acoustic Pulsations in Gas Transport Systems: Experimental Study of the Influence of Closed Side Branches," *Journal of Sound and Vibration*, Vol. 150, 1991, pp. 371–394.

[24]Durrieu, P., Hofmans, G., Ajello, G., Boot, R., Auregan, Y., Hirschberg, A., and Peters, M. C. A. M., "Quasi-Steady Aero-Acoustic Response of Orifices," *Journal of the Acoustical Society of America*, Vol. 110, 2001, pp. 1859–1872.

[25]Bruggeman, J. C., Hirschberg, A., Van Dongen, M. E. H., Wijnands, A. P. J., and Gorter, J., "Flow Induced Pulsations in Gas Transport Systems: Analysis of the Influence of Closed Side Branches," *Journal of Fluids Engineering*, Vol. 111, 1989, pp. 484–491.

[26]Tam, C. K. W., and Kurbatskii, K. A., "Microfluid Dynamics and Acoustics of Resonant Liners," *AIAA Journal*, Vol. 38, No. 8, 2000, pp. 1331–1339.

[27]Temkin, S., *Elements of Acoustics*, Wiley, New York, 1981, pp. 177–180.

[28]*Fluid Meters—Their Theory and Applications*, American Society of Mechanical Engineers, New York, 1959.

[29]Schlichting, H., *Boundary-Layer Theory*, McGraw–Hill, New York, 1968, pp. 176–178, 560.

[30]Rosenhead, L. (ed.), *Laminar Boundary Layers*, Clarendon, Oxford, 1963, pp. 134, 135, 439–446.

[31]Jones, M. G., and Steide, P. E., "Comparison of Methods for Determining Specific Acoustic Impedance," *Journal of the Acoustical Society of America*, Vol. 5, Pt. 1, May 1997, pp. 2694–2704.

[32]Thurston, G. B., and Martin, C. E., "Periodic Fluid Flow Through Circular Orifices," *Journal of the Acoustical Society of America*, Vol. 25, No. 1, 1953, pp. 26–31.

[33]Bies, D. A., and Wilson, O., Jr., "Acoustic Impedance of a Helmholtz Resonator at Very High Amplitude," *Journal of the Acoustical Society of America*, Vol. 29, No. 1, 1957, pp. 711–714.

[34]Innes, D., and Creighton, D., "On a Non-Linear Differential Equation Modeling Helmholtz Resonator Response," *Journal of Sound and Vibration*, Vol. 131, No. 2, 1989, pp. 323–330.

H. M. Atassi
Associate Editor